ACS APPLIED MATERIALS & INTERFACES

Research Article

www.acsami.org

Morphology-Controlled Synthesis of Self-Assembled $LiFePO_4$/C/RGO for High-Performance Li-Ion Batteries

Mei Lin,[†] Yuming Chen,[‡] Bolei Chen,[†] Xiao Wu,[†] Kifung Kam,[†] Wei Lu,[†] Helen Lai Wa Chan,[†] and Jikang Yuan*[,†]

[†]Department of Applied Physics and Materials Research Centre, The Hong Kong Polytechnic University, Hong Kong, China

[‡]Department of Mechanical Engineering, The Hong Kong Polytechnic University, Hong Kong, China

Supporting Information

ABSTRACT: Novel architectured $LiFePO_4$ (LFP) that consisted of ordered LFP nanocubes was prepared through a facile hydrothermal method using polyethylene glycol (PEG) as a surfactant. The micro/nanostructured LFP with various morphologies ranging from cube cluster to rugby-like structure was synthesized via controlling the pH values of the precursor. A reasonable assembly process elucidating the formation of the hierarchical structure is also provided based on the experimental results. After a combination of carbon (C) coating and reduced graphene oxide (RGO) wrapping, the obtained LFP/C/RGO composites exhibit enhanced electrochemical performance compared to that of blank LFP synthesized under the same condition. Among as-synthesized cube-cluster-like, dumbbell-like, rod-like, and rugby-like composites, the rugby-like LFP/C/RGO reveal the best electrochemical properties with the discharge specific capacity of ~150 mA h g^{-1} after 100 cycles and a high reversible specific capacity of 152 mA h g^{-1} at 0.1 C. The prepared LFP/C/RGO composite can be a promising cathode material for high energy, low cost, and environmentally friendly lithium-ion batteries.

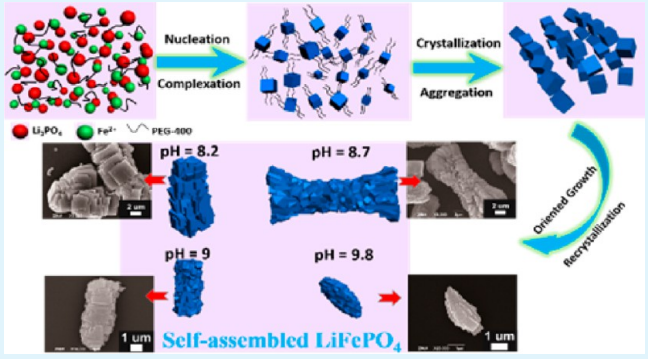

KEYWORDS: *$LiFePO_4$, self-assembled, hydrothermal, reduced graphene oxide, Li-ion batteries*

INTRODUCTION

With the ever-growing demands for portable electronics and environmental-benign devices, rechargeable lithium ion batteries (LIBs) have attracted considerable attention owing to their outstanding performances, such as high energy density, good cyclability, and portability.[1−3] Olivine-type $LiFePO_4$ (LFP) has been regarded as one of the most promising cathode materials for power batteries in electric vehicles (EVs), as it has a high theoretical specific capacity (170 mA h g^{-1}), low cost, environmental compatibility, and superb stability.[4−7] However, the achievement of wide applications in powerful LIBs was significantly restricted by poor electrical conductivity and sluggish lithium-ion transport.[8−10] Tremendous efforts have been made to improve LFP electrode performance by coating electronically conductive agents,[11−15] doping with foreign atoms,[16−20] or reducing the LFP particle size.[21,22] It is evident that the nanostructure facilitates shorter ion diffusion paths, which allows for efficient ion transport, thereby leading to improved electrochemical performance.[23] Nevertheless, the highly performing nanostructure LFP suffers from low tap density and volumetric energy density limitations.[7] Thus, to overcome these drawbacks, extensive studies have been initiated to explore novel LFP nanostructures.

By combining the advantages of nanoscaled building blocks and microscaled assemblies, the novel hybrid with self-assembled nano/micro structures are highly pursued for improving the lithium storage properties.[24−26] Thus, constructing desirable LFP architectures by self-assembling nanoscale building blocks is becoming an intensive and hot research topic. In recent years, many research efforts have been focused on developing various LFP synthetic techniques and products with multifarious self-assembled morphologies, including spindle-like,[27] dumbbell-like,[28] hollow spherical[29] and nano/microspheres.[25,30] From a review of previous studies, the electrochemical properties and practical or potential applications strongly depend on the morphology and size of LFP. The control of morphology is an effective approach to determine the size/structure-dependent properties.[31] However, controlling the morphology of the resulting materials remains an issue. Hence, further improvement of electrochemical performance of LFP still requires an optimization of the synthetic strategies to produce LFP with well-defined morphology and size.

Received: May 28, 2014
Accepted: September 18, 2014
Published: September 18, 2014

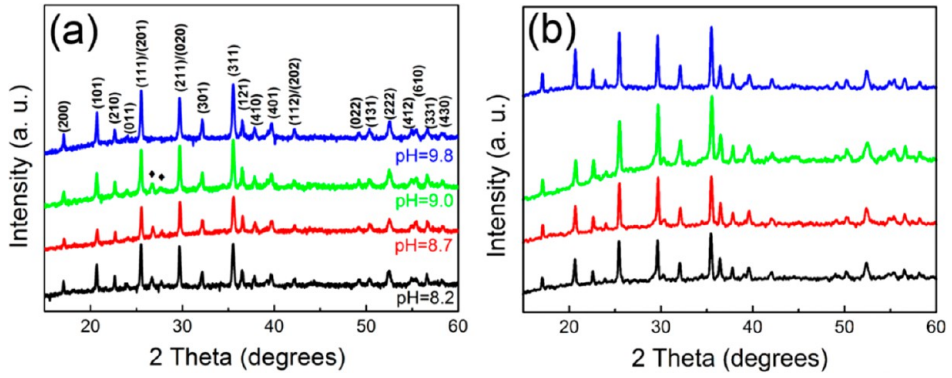

Figure 1. XRD patterns of various prepared LFP samples from different pH values in the precursors (a) before and (b) after annealing.

Hydrothermal synthesis offers many advantages, such as simplicity, cost effectiveness, good morphology control, and low working temperature.[32] Accordingly, the hydrothermal synthetic approach is widely used to prepare LFP.[28,33] The pH value of the precursor solution plays a key role on the influence of the morphology and size of the prepared materials during the hydrothermal process. Many recent efforts have been focused on the morphology control by adjusting the pH values of the precursor.[32] Here we systematically investigated the effect of pH values on the self-assembly LFP structure. The particle morphology, crystal orientation, and electrochemical properties of the prepared nanostructured LFP were also investigated. After combination of carbon coating and reduced graphene oxide (RGO) wrapping, the capacity of about 150 mA h g^{-1} was obtained based on the LFP/C/RGO composites.

EXPERIMENTAL SECTION

Synthesis of LFP. The LFP samples were prepared by a simple hydrothermal method in an autoclaved stainless steel reaction vessel. All the chemicals used were purchased without further purification. A stoichiometric mixture of lithium hydroxide monohydrate ($LiOH{\cdot}H_2O$), iron sulfate heptahydrate ($FeSO_4{\cdot}7H_2O$), and phosphoric acid (H_3PO_4) was mixed in a 2:1:1 molar ratio. First, PEG-400 (mean molecular weight of 380−420) was dispersed in deionized (DI) water under constantly stirring for 6 h to obtain a homogeneous and transparent solution. $FeSO_4{\cdot}7H_2O$ and H_3PO_4 were dissolved in DI water simultaneously, and then quickly added to the PEG solution. Subsequently, $LiOH{\cdot}H_2O$ was slowly added into the above mixture with moderate stirring for 10 min. The pH value of the precursor suspension was adjusted by ammonia solution ($NH_3{\cdot}nH_2O$). Finally, a blue-green suspension was transferred into a Teflon-lined stainless steel autoclave and then heated at 190 °C for 12 h. The autoclave was subsequently cooled to room temperature and the resulting green precipitate was collected from the autoclave and then washed, filtered, and dried at 60 °C overnight.

Preparation of LFP/C/RGO Composites. Graphene oxide (GO) sheets were synthesized from graphite powder (Aldrich, powder, synthetic) using the modified Hummers method.[34] The resulting GO sheets were dispersed in DI water (20 mL) by ultrasonication for 30 min, then centrifuged (4000 rpm, 30 min) to remove residual GO. Emulsifier OP-10 ($C_{34}H_{62}O_{11}$) was dispersed in DI water (20 mL) via strong agitation for 12 h; after that, the obtained LFP powders were added into the emulsifier OP-10 solution. After the solution was stirred for 6 h, the GO (the weight ratio of GO/LFP was 7%) solution was added into the above suspension and the resulting solution was kept stirring for 2 h. To reduce GO, the hydrazine was dropped into the mixture solution, followed by stirring at 80 °C to evaporate the solvent. Finally, the powder was annealed in a tube furnace at 650 °C for 2 h (heating rate of 5 °C/min) under N_2 (95%)/H_2 (5%) to obtain LFP/C/RGO composites.

Characterization and Electrochemical Measurements. The phase purity and crystalline structure of the as-obtained samples were characterized by X-ray powder diffraction (XRD) (Rigaku SmartLab) equipped with Cu Kα radiation operated at 45 kV and 200 mA. The morphology and particle size of the products were observed by scanning electron microscopy (SEM, JEOL Model JSM-6490) and transmission electron microscopy (TEM, JEOL JEM-2100F). The building blocks of the microstructure samples were determined using a high-resolution TEM (HRTEM) on a JEM-2100F apparatus with an acceleration voltage of 200 kV. Raman measurements were performed using Raman spectroscopy (HORIBA JOBIN YVON, HR800) with the laser wavelength of 488 nm.

Electrochemical properties were measured using 2032 coin-type half-cells that were assembled in an argon-filled glovebox. A mixture of LFP/C/RGO composite, acetylene black, and poly(vinyl difluoride) (PVDF) at a weight ratio of 70:20:10 was uniformly pasted onto Al foil. The electrodes were dried at 60 °C for 6 h followed by roll-pressing and further drying at 60 °C for 12 h in a vacuum oven before assembly. A polypropylene film (Cellgard 2400) was used as a separator, and pure lithium foil was employed as the negative electrode. One molar $LiPF_6$ was dissolved in a 1:1 mixture of ethylene carbonate (EC) and dimethyl carbonate (DMC) to form the electrolyte. Galvanostatic charge/discharge measurement of assembled cells was performed by the Land Battery Test System (CT2001A, Wuhan Land Electronic Co. Ltd., China) in the voltage range of 2.3−4.2 V with various current densities at room temperature.

RESULTS AND DISCUSSION

The XRD measurements were carried out to confirm the composition of the as-prepared various synthesized LFP samples from different pH values, as shown in Figure 1a. All the samples can be well indexed to the orthorhombic olivine-type structure (JCPDS No. 40-1499). Clearly, there are two peaks for Fe_2PO_5 (JCPDS No. 36-84) in the prepared materials with low pH values of the precursor solution (8.2, 8.7, and 9.0),[35] as marked in Figure 1a (2θ between 25°−30°). However, these peaks for Fe_2PO_5 are not observed and pure orthorhombic LFP is obtained from a high pH of 9.8 in the

precursor solution, which suggests that high pH is beneficial for the preparation of pure LFP. After subsequent heat treatment, the peaks of Fe_2PO_5 disappear (Figure 1b) while the diffraction peaks of the crystalline LFP phase still remain.

To study the morphology evolution of the obtained LFP structures, the SEM images of various resultant LFP samples under different pH conditions are displayed in Figure 2. It is found that the morphologies of the LFP change from cube-cluster-like to rugby-like shape with the increase of pH values. The obtained sample is entirely composed of microstructures built from cubes when the pH is fixed at 8.2 (Figure 2a). In the high-magnification SEM image (Figure 2b), the cube units with the length ranging from 1 to 2 μm assemble into cube clusters with the length of ~6 μm. The self-assembly and cross-linked cubes form a hierarchical microstructure. When the pH value is increased to 8.9, an interesting dumbbell-like LFP with the length of ~15 μm and width of 6−8 μm can be obtained (Figure 2c). Moreover, the high-magnification SEM image (Figure 2d) shows that the middle section of dumbbell-like microstructure is composed of many nanoparticles while both ends are microparticles.

As shown in Figure 2e, rod-like microstructures with lengths ranging from 6 to 7 μm and widths of 2−3 μm can be achieved by further increasing the pH values. Figure 2f shows the SEM image of rod-like nanostructured LFP and the inset of Figure 2f displays an individual rod-like LFP, showing that the LFP rod-like nanostructure is hierarchically constructed with many nanocubes. These tiny building blocks are assembled side by side in an ordered arrangement. The low- and high-magnification SEM images of the products obtained from the precursor solution at pH = 9.8 are given in Figure 2g,h. The low-magnification SEM image (Figure 2g) shows the rugby-like morphology. The high-magnification image (Figure 2h) exhibits that the typical length and width of the rugby are in the ranges of 3−4 and 0.4−2 μm, respectively. The inset of Figure 2h reveals that the rugby-like nanostructure consists of irregular nanocubes with the size of 200−300 nm, which is close to the size calculated from the XRD analysis (180 nm). These above morphological studies indicate that the pH values of precursor solution remarkably affect both the morphology and grain size of LFP. The higher pH value results in the smaller LFP particle size.

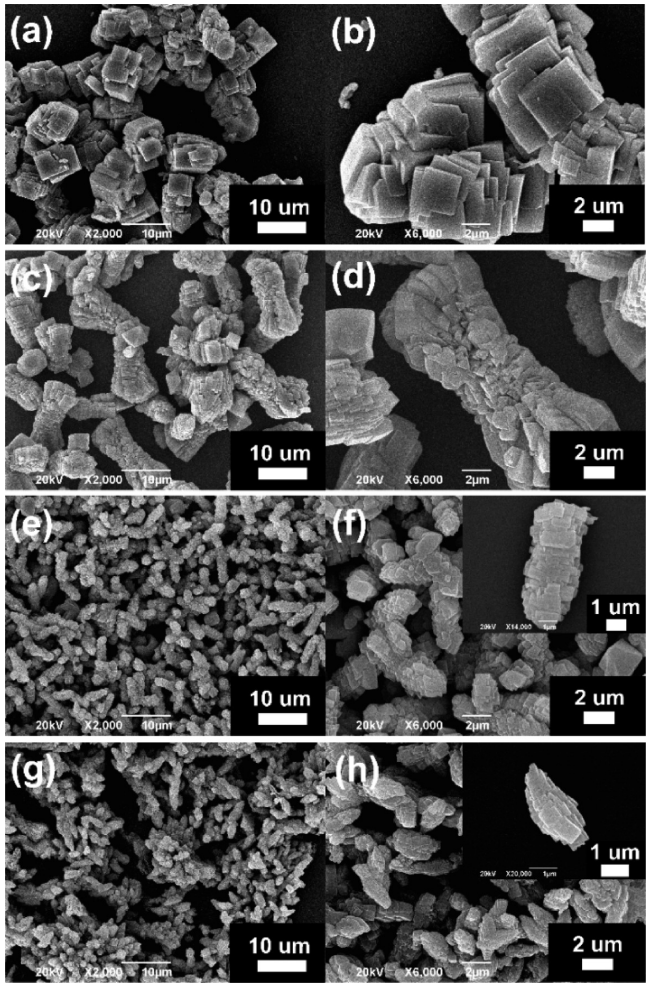

Figure 2. SEM images of various LFP samples from the precursors with different pH values. (a, b) pH = 8.2, (c, d) pH = 8.7, (e, f) pH = 9.0, and (g, h) pH = 9.8.

The typical TEM and HRTEM images, and corresponding selected area electron diffraction (SAED) patterns of an individual building block of LFP were performed in Figure 3. TEM images (Figure 3a,c,e,g) illustrates that the morphology and size of LFP obtained from precursors with different pH values are well consistent with those from the SEM images. The HRTEM image (Figure 3b) of cube clusters LFP exhibits clear lattice fringes, indicating a well-crystallized structure of the orthorhombic LFP product. The *d*-spacing values of the

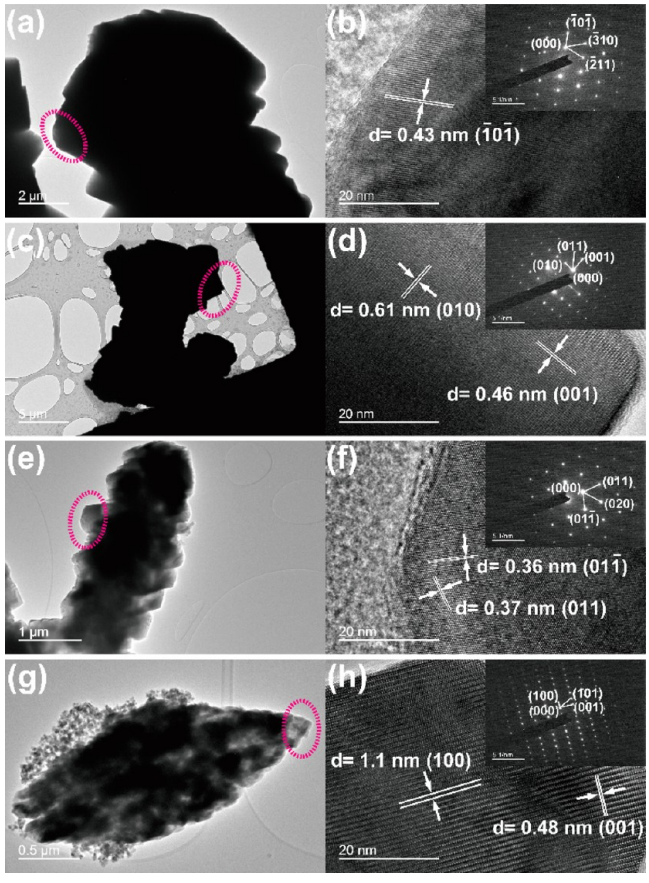

Figure 3. Typical TEM images, HRTEM images, and SAED patterns (inset in HRTEM images) of the LFP samples for different morphologies. (a, b) Cube-cluster-like, (c, d) dumbbell-like, (e, f) rod-like, and (g, h) rugby-like.

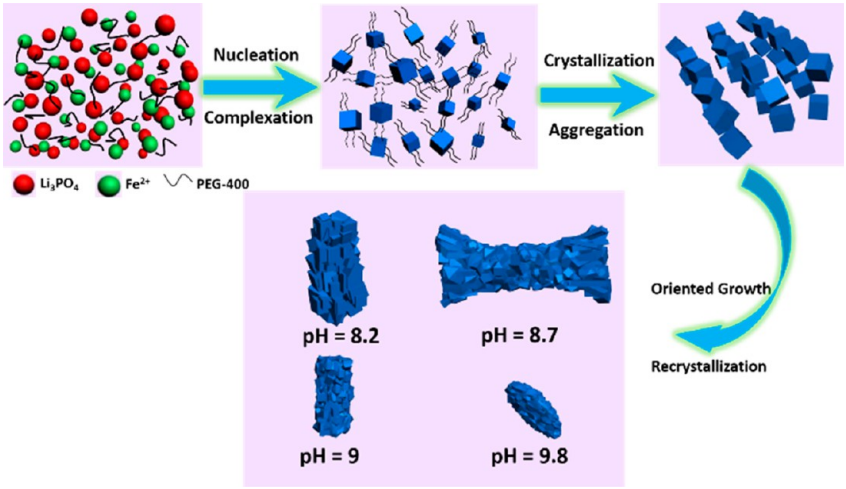

Figure 4. Schematic illustration for the formation mechanism of various self-assembled LFP samples during the hydrothermal reaction.

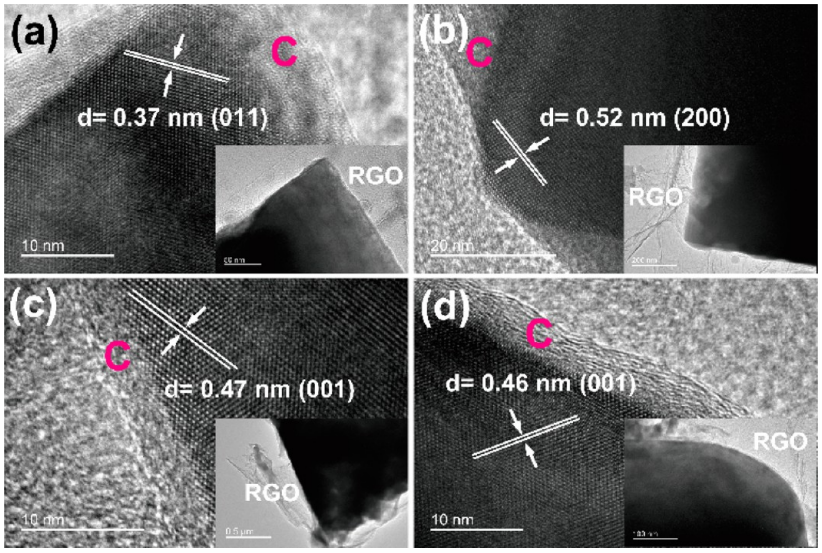

Figure 5. HRTEM images and TEM images (inset) of the LFP/C/RGO composites. (a) Cube-cluster-like, (b) dumbbell-like, (c) rod-like, (d) rugby-like structures.

adjacent lattice planes are 0.43 nm, corresponding to the $(\bar{1}0\bar{1})$ planes of orthorhombic LFP. The inset of Figure 3b confirms that these self-assembled cubes are indeed a pure crystalline phase, and the SAED pattern corresponds to the $(\bar{1}0\bar{1})$, $(\bar{3}10)$, and $(\bar{2}11)$ planes. Figure 3d shows the crystal lattices of dumbbell-like LFP with *d*-spacing of approximately 0.61 and 0.46 nm, corresponding to the (010) and (001) crystal faces. The diffraction spots (inset of Figure 3d) are determined to the (010), (011), and (001) planes, respectively. The clearly arrayed spots in the SAED pattern suggest that the prepared dumbbell-like LFP is highly crystalline. The HRTEM images of rod-like LFP in Figure 3f shows two sets of clear lattice fringes, with the widths of 0.36 and 0.37 nm, which are from the $(01\bar{1})$ and (011) planes. The diffraction spots (inset of Figure 3f) can be uniformly indexed to the (011), (020), and $(01\bar{1})$ planes of orthorhombic LFP, indicating that the sample is high crystalline and pure phase. Figure 3g displays a typical TEM image of rugby-like LFP aggregate stacked by irregular nanoparticles. The clear lattice fringes (Figure 3h) represent the single crystallinity, and the width of 1.1 and 0.48 nm of the neighboring lattice fringes are comparable to the result of SAED (inset of Figure 3h) for the reflection (100) and (001) plane of LFP. The above results are well coincided with the XRD patterns.

Figure 4 illustrates the suggested evolving mechanism for the formation of self-assembled micro/nanostructured LFP on the effect of pH value. The formation process can be illustrated by the dissolution-recrystallization mechanism. First, the reactants (Li_3PO_4 precipitation, Fe^{2+}, and PEG-400) are mixed during the hydrothermal reaction and a large number of Li_3PO_4 precipitations start to form LFP crystalline nuclei.[28] Then PEG is possible to be adsorbed on the surface of each LFP nuclei, which quickly grows to cubic-shaped LFP nanocrystals. Because of the driving force of the minimization of surface area, small primary nanocrystals can self-assemble into more stable cubes. With a prolonged reaction time, LFP cubes further oriented an aggregate to constitute a 3D structure to decrease the surface energy. After dissolution and recrystallization under different concentrations of ammonium ions (pH values), these LFP cubes assemble in the side-by-side and cross-linked growth manner and subsequently rearrange to form four types of self-assembled structures, including assembled cube-clusters-like,

dumbbell-like, rod-like, and rugby-like morphologies. The differences among the morphologies of the four samples (Figure 4) can be attributed to crystal growth rates in various pH values. It is generally known that the solubility of the solute can directly affect the rate of crystal growth in solution. At a relatively low pH value (pH = 8.2 and 8.7), the high solubility of precursors always results in the high crystals growth rates.[36] Then, the crystals and assemblages with large size are preferentially formed. Under strongly alkaline conditions (pH = 9 and 9.8), shielding effect can be generated by OH^- ions at the interface that will slow down the growth rate of various faces during the crystallization process.[37] So the nucleation process is probable to be a dominant factor over the crystal growth, resulting in crystals and assemblages with small size.

To enhance the conductivity of the LFP material applied in Li-ion battery, the LFP/C/RGO composited structure was obtained. The morphologies of the composites were examined by SEM (Figure S1, Supporting Information) shows that the comodification of LFP with a RGO and carbon coating constructed an effective conducting network. The LFP and RGO were connected by carbon, while the LFP samples were covered by RGO sheet that acted as the conducting medium. The morphologies of our four LFP/C/RGO samples still retain their original shapes (a, b, cube-cluster-like; c, d, dumbbell-like; e, f, rod-like; g, h, rugby-like) as compared with those in Figure 2. As shown in the high resolution images (Figure S1b,d,f,h, Supporting Information) the cube-cluster-like and dumbbell-like LFP are incompletely wrapped by C/RGO, while the rod-like and rugby-like LFP with the smaller size are completely wrapped by C/RGO. These SEM results are consistent with the results of the TEM measurements (Figure 3). TEM and HRTEM were employed to confirm and characterize the microstructure of LFP/C/RGO composites. As shown in Figure 5, some LFP building blocks are wrapped by RGO sheets. The HRTEM image taken from the edge of cube-cluster-like LFP displays clear crystal lattices with *d*-spacing of 0.37 nm, corresponding to the (011) planes of orthorhombic phase LFP (Figure 5a). The surface of the product is coated by carbon layer with a thickness of 5−8 nm. Figure 5b shows the HRTEM image of dumbbell-like LFP/C/RGO composite. It can be seen that an amorphous carbon coating layer with an uneven thickness is covered on the surface of LFP. The clear lattice fringes with interplanar spacing of 0.52 nm can be assigned to the (200) plane of LFP. Figure 5c shows the HRTEM image of the rod-like LFP/C/RGO hybrid with interplanar spacing of 0.47 nm corresponding to the (001) plane of LFP. An amorphous carbon layer with a thickness of 5 nm on the LFP can also be observed. A HRTEM image (Figure 5d) from the edge of the rugby-like LFP reveals that the LFP grains are wrapped by a uniformly thin film of graphitized carbon with a thickness of 6 nm. It also shows clear crystal planes with a *d*-spacing of 0.46 nm, corresponding to the (001) planes of orthorhombic LFP. The above-mentioned results indicate that rod-like and rugby-like LFP/C/RGO composites possess thinner and more uniform carbon coating layer as compared with two other as-prepared LFP/C/RGO composites. During the carbon coating process, emulsifier OP-10 acts not only as a surfactant but also as the carbon source for carbon coating. Therefore, the LFP particles and RGO are connected by these coated carbons, forming an effective conducting network that dramatically improves the electronic conductivity of LFP. The TEM results are well consistent with the SEM images (Figure S1, Supporting Information).

We further analyzed the Raman spectra of LFP/C/RGO composites with different morphologies, as shown in Figure 6.

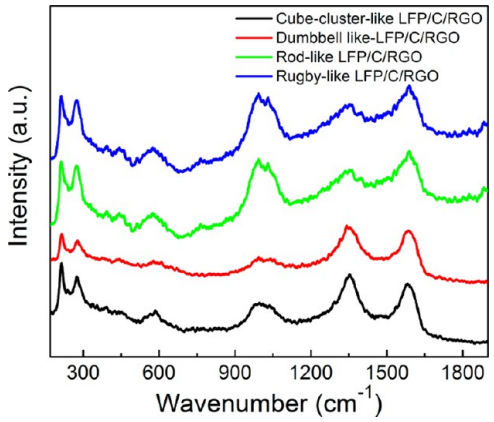

Figure 6. Raman spectra of various self-assembled LFP/C/RGO composites.

The bands in the ranges of 200−500 and 520−1170 cm^{-1} are observed in the four as-prepared LFP/C/RGO composites, which could be assigned to the Raman vibrations of Fe−O and PO_4^{3-} characteristic intramolecular stretching modes.[38] The weak peaks in the 520−1170 cm^{-1} region for cube clusters and dumbbell-like LFP/C/RGO composites are ascribed to the poor crystallinity of LFP. The band at 1351 cm^{-1} corresponds to the D-band (disorder-induced phonon mode) of carbon, and the band at 1590 cm^{-1} is assigned to the G-band showing the presence of the graphitic carbon.[39] The I_D/I_G, disordered/graphitic ratio, is commonly used to evaluate the disorder degree in graphitic materials.[40] The lower value means a larger quantity of graphitized carbon. It is obvious that the I_D/I_G ratio of the rod-like and rugby-like LFP/C/RGO composites is lower than that of others. Namely, the rod-like and rugby-like composites show a higher degree of graphitization. It is widely accepted that the smaller particles possess a larger specific surface area, leading to closer contact with reduced graphene oxide. Therefore, the rod-like and rugby-like LFP tend to be mixed more closely with reduced graphene oxide, compared with their counterpart with larger particles. This conclusion is also supported by the HRTEM results (Figure 5).

Figure 7a shows the typical galvanostatic charge/discharge voltage profiles of the initial 20 cycles for the rugby-like LFP/C/RGO composite at 0.1 C. In the first cycle, the discharge specific capacity is 127 mA h g^{-1}. The specific capacity approaches an optimal value of about 150 mA h g^{-1} after the 20th cycle. Because it is difficult for the binder to soak and absorb the electrolyte and the LFP are not fully activated in the first few cycles, but the Li-ion transport channel can be extended as the charge/discharge cycling progresses, thus activating the remainder of LFP.[41] Figure 7b shows the charge/discharge curves of the as-prepared LFP/C/RGO composites at 0.1 C after 50 cycles. The cathodes made from the self-assembled rod-like and rugby-like LFP/C/RGO composites exhibit rather higher discharge capacities than that of the cube-cluster-like and dumbbell-like LFP/C/RGO composites. The cycle discharge capacities for the four typical LFP/C/RGO composites are 56, 97, 140, and 155 mA h g^{-1}, respectively. The curves exhibit a typical plateau at approximately 3.4 V (versus Li^+/Li), implying a two phase Fe^{3+}/Fe^{2+} redox reaction for the electrodes. The small voltage difference between the plateaus of

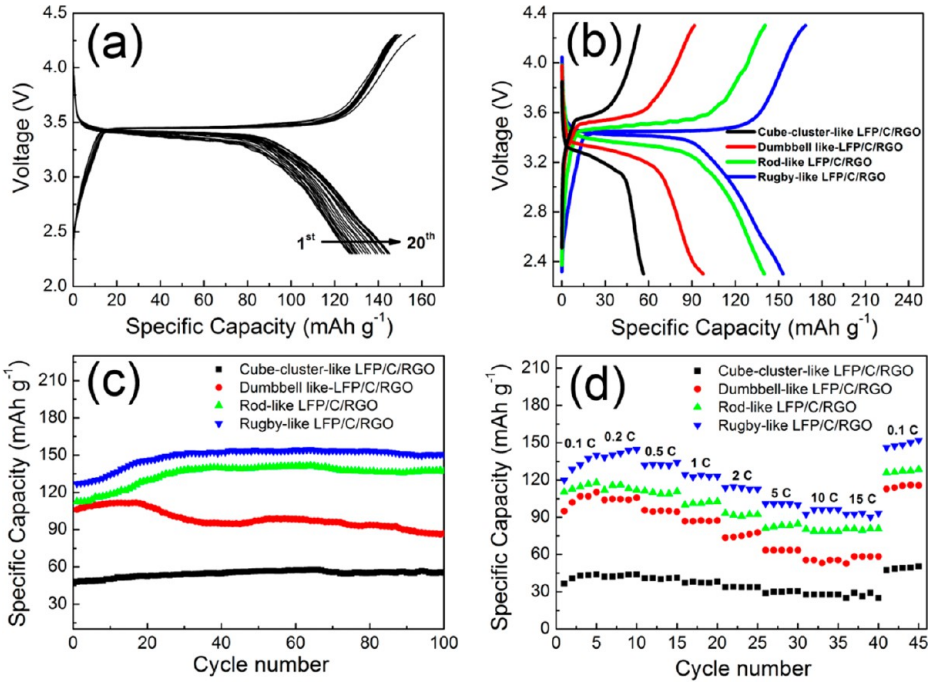

Figure 7. Electrochemical characterizations of the LFP/C/RGO composites in the voltage range of 2.3−4.2 V (versus Li^+/Li). (a) Glavanostatic charge/discharge voltage profiles at 0.1 C (1C = 170 mA g^{-1}) for the first 20 cycles for rugby-like LFP/C/RGO composite. (b) Charge/discharge curves for the 51 cycle at a current rate of 0.1 C. (c) Cycling profiles tested at a current density of 0.1 C. (d) Rate performance of the composites.

the charge−discharge potential for the rugby-like LFP/C/RGO composites indicates the superior electrochemical kinetics.[42] To further understand the electrochemical performance of LFP, the long cycling performance of the LFP/C/RGO composites were investigated at a current rate of 0.1 C between 2.3 and 4.2 V, as illustrated in Figure 7c. As expected, both the self-assembled rod-like and rugby-like LFP/C/RGO composites possess higher initial capacities than those of the dumbbell-like and cube-cluster-like LFP/C/RGO composites. No obvious fade can be observed in rod-like and rugby-like samples after 100 cycles. However, the discharge capacity of dumbbell-like sample fades significantly after 20 cycles and retains only 97 mA h g^{-1} after 100th cycles. Low discharge capacity of 50 mA h g^{-1} is observed for cube-cluster-like LFP/C/RGO sample. Compared with the cube-cluster-like and dumbbell-like LFP/C/RGO composites, the rod-like and rugby-like ones display much better lithium intercalation/deintercalation performance. Additionally, the rugby-like LFP/C/RGO sample shows the superior rate capability (Figure 7d). The reversible capacity of electrode regains to 152 mA h g^{-1} when the current rate returns to 0.1 C after 40 cycles, indicating an excellent rate capability. The reversible capacities of cube-cluster-like, dumbbell-like and rod-like LFP/C/RGO composites are 50, 116, and 129 mA h g^{-1}, respectively. These results reveal that the rugby-like LFP/C/RGO composites possess the best electrochemical performance. Figure S2 (Supporting Information) shows the cycling performance of the rod-like and rugby-like LFP/C/RGO composites at charge−discharge currents of 10 C. For the rugby-like LFP/C/RGO, a capacity of 107 mA h g^{-1} still can be obtained at a high current rate of 10 C, confirming the high stability of the rugby-like LFP/C/RGO composite for high rates of charge−discharge. According to the HRTEM (Figure 5) and Raman (Figure 6) results, the rod-like and rugby-like LFP/C/RGO composites are covered by a uniform thinner carbon film and contain a larger amount of graphitized carbon that can significantly enhance the electrical conductivity. Therefore, rod-like and rugby-like LFP/C/RGO composites exhibit better cycle performances. Furthermore, the electrochemical performance is related to the diffusion rate of Li ions. The nanosized building blocks can reduce the Li ions diffusion distance, leading to the improvement of the Li ions diffusion rate. Among the four samples, the rugby-like LFP has the smallest average size of building blocks (Figure 2), which facilitates the diffusion of Li ions, resulting in the best electrochemical performance.

CONCLUSION

In summary, various self-assembled hierarchical micro/nanostructured LFP samples were successfully prepared by a facile hydrothermal synthesis method using PEG-400 as the surfactant. Simultaneously, by controlling the pH values ranging from 8.2 to 9.8, different morphologies of LFP (including cube-cluster-like, dumbbell-like, rod-like, and rugby-like architectures) can be achieved. These results indicate that pH value plays an important role in construction of the hierarchically self-assembled micro/nanostructures. After the combination of carbon coating and RGO wrapping treatment, the rugby-like LFP/C/RGO electrode exhibits a rather higher discharge capacity and a better rate capability when compared with those of the other two as-prepared composites of LFP. The excellent electrochemical properties are probably attributed to the unique hierarchical structures and superior conducting networks consisting of RGO and coated carbon. The simple methodology presented here may pave a new path for the large-scale preparation of phospholivine-type anode materials such as $LiMPO_4$ (M = Mn, Co, Ni, etc.).

■ ASSOCIATED CONTENT

Supporting Information

SEM image of the LFP/C/RGO samples; cycling performance for rod-like LFP/C/RGO and rugby-like LFP/C/RGO composites at a current rate of 10 C. This material is available free of charge via the Internet at http://pubs.acs.org.

■ AUTHOR INFORMATION

Corresponding Author

*J. Yuan. E-mail: jikang.yuan@polyu.edu.hk. Fax: +852 2333 7629. Tel: +852 2766 5685.

Notes

The authors declare no competing financial interest.

■ ACKNOWLEDGMENTS

This work is supported in part by Hong Kong Government General Research Fund (Grant No. B-Q30V), the Hong Kong Polytechnic University Grant Research Committee Funds (Grant No.s A-PL52, 1-ZV9B and 1-ZV5K).

■ REFERENCES

(1) Armand, M.; Tarascon, J. M. Building Better Batteries. *Nature* **2008**, *451*, 652−657.

(2) Maier, J. Nanoionics: Ion Transport and Electrochemical Storage in Confined Systems. *Nat. Mater.* **2005**, *4*, 805−815.

(3) Li, H.; Wang, Z.; Chen, L.; Huang, X. Research on Advanced Materials for Li-Ion Batteries. *Adv. Mater.* **2009**, *21*, 4593−4607.

(4) Padhi, A.; Nanjundaswamy, K.; Goodenough, J. B. Phospho-Olivines as Positive-Electrode Materials for Rechargeable Lithium Batteries. *J. Electrochem. Soc.* **1997**, *144*, 1188−1194.

(5) Chung, S. Y.; Bloking, J. T.; Chiang, Y. M. Electronically Conductive Phospho-Olivines as Lithium Storage Electrodes. *Nat. Mater.* **2002**, *1*, 123−128.

(6) Gibot, P.; Casas-Cabanas, M.; Laffont, L.; Levasseur, S.; Carlach, P.; Hamelet, S.; Tarascon, J. M.; Masquelier, C. Room-Temperature Single-Phase Li Insertion/Extraction in Nanoscale Li_xFePO_4. *Nat. Mater.* **2008**, *7*, 741−747.

(7) Sun, C. W.; Rajasekhara, S.; Goodenough, J. B.; Zhou, F. Monodisperse Porous $LiFePO_4$ Microspheres for a High Power Li-Ion Battery Cathode. *J. Am. Chem. Soc.* **2011**, *133*, 2132−2135.

(8) Arico, A. S.; Bruce, P. G.; Scrosati, B.; Tarascon, J. M.; Schalkwijk, W. V. Nanostructured Materials for Advanced Energy Conversion and Storage Devices. *Nat. Mater.* **2005**, *4*, 366−377.

(9) Amin, R.; Balaya, P.; Maier, J. Anisotropy of Electronic and Ionic Transport in $LiFePO_4$ Single Crystals. *Electrochem. Solid-State Lett.* **2007**, *10*, A13−A16.

(10) Saravanan, K.; Reddy, M. V.; Balaya, P.; Gong, H.; Chowdari, B. V. R.; Vittal, J. J. Storage Performance of $LiFePO_4$ Nanoplates. *J. Mater. Chem.* **2009**, *19*, 605−610.

(11) Oh, S. W.; Myung, S. T.; Oh, S. M.; Oh, K. H.; Amine, K.; Scrosati, B.; Sun, Y. K. Double Carbon Coating of $LiFePO_4$ as High Rate Electrode for Rechargeable Lithium Batteries. *Adv. Mater.* **2010**, *20*, 4842−4845.

(12) Kim, W. K.; Ryu, W. H.; Han, D. W.; Lim, S. J.; Eom, J. Y.; Kwon, H. S. Fabrication of Graphene Embedded $LiFePO_4$ Using a Catalyst Assisted Self Assembly Method as a Cathode Material for High Power Lithium-Ion Batteries. *ACS Appl. Mater. Interfaces* **2014**, *6*, 4731−4736.

(13) Hu, Y. S.; Guo, Y. G.; Dominko, R.; Gaberscek, M.; Jamnik, J.; Maier, J. Improved Electrode Performance of Porous $LiFePO_4$ Using RuO_2 as an Oxidic Nanoscale Interconnect. *Adv. Mater.* **2007**, *19*, 1963−1966.

(14) Lee, Y. C.; Han, D. W.; Park, M. H.; Jo, M. R.; Kang, S. H.; Lee, J. K.; Kang, Y. M. Tailored Surface Structure of $LiFePO_4$/C Nanofibers by Phosphidation and Their Electrochemical Superiority for Lithium Rechargeable Batteries. *ACS Appl. Mater. Interfaces* **2014**, *6*, 9435−9441.

(15) Hasegawa, G.; Ishihara, Y.; Kanamori, K.; Miyazaki, K.; Yamada, Y.; Nakanishi, K.; Abe, T. Facile Preparation of Monolithic $LiFePO_4$/Carbon Composites with Well-Defined Macropores for a Lithium-Ion Battery. *Chem. Mater.* **2011**, *23*, 5208−5216.

(16) Chung, S. Y.; Kim, J. G.; Kim, Y. M.; Lee, Y. B. Three-Dimensional Morphology of Iron Phosphide Phases in a Polycrystalline $LiFePO_4$ Matrix. *Adv. Mater.* **2011**, *23*, 1398−1403.

(17) Tong, D. G.; Li, Y. L.; Chu, W.; Wu, P.; Luo, F. L. Preparation and Characterization of $LiFe_{0.975}Rh_{0.025}PO_4$ Nanorods Using Uhehydrothermal Method. *Dalton Trans.* **2011**, *40*, 4087−4094.

(18) Yang, G.; Jiang, C. Y.; He, X. M.; Ying, J. R.; Cai, F. P. Preparation of V-$LiFePO_4$ Cathode Material for Li-Ion Batteries. *Ionics* **2012**, *18*, 59−64.

(19) Bilecka, I.; Hintennach, A.; Rossell, M. D.; Xie, D.; Novak, P.; Niederberger, M. Microwave-Assisted Solution Synthesis of Doped $LiFePO_4$ with High Specific Charge and Outstanding Cycling Performance. *J. Mater. Chem.* **2011**, *21*, 5881−5890.

(20) Yang, J. L.; Wang, J. J.; Li, X. F.; Wang, D. N.; Liu, J.; Liang, G. X.; Gauthier, M.; Li, Y. L.; Geng, D. S.; Li, R. Y.; Sun, X. L. Hierarchically Porous $LiFePO_4$/Nitrogen-Doped Carbon Nanotubes Composite as a Cathode for Lithium Ion Batteries. *J. Mater. Chem.* **2012**, *22*, 7537−7543.

(21) Jiang, J.; Liu, W.; Chen, J. T.; Hou, Y. L. $LiFePO_4$ Nanocrystals: Liquid-Phase Reduction Synthesis and Their Electrochemical Performance. *ACS Appl. Mater. Interfaces* **2012**, *4*, 3062−3068.

(22) Manthiram, A.; Murugan, A. V.; Sarkar, A.; Muraliganth, T. Nanostructured Electrode Materials for Electrochemical Energy Storage and Conversion. *Energy Environ. Sci.* **2008**, *1*, 621−638.

(23) Wang, Y. G.; Wang, Y. R.; Hosono, E.; Wang, K. X.; Zhou, H. S. The Design of a $LiFePO_4$/Carbon Nanocomposite with a Core-Shell Structure and Its Synthesis by an In Situ Polymerization Restriction Method. *Angew. Chem., Int. Ed.* **2008**, *47*, 7461−7465.

(24) Liu, Y. M.; Chen, B. L.; Cao, F.; Zhao, X. Z.; Yuan, J. K. Synthesis of Nanoarchitectured $LiNi_{0.5}Mn_{0.5}O_2$ Spheres for High-Performance Rechargeable Lithium-Ion Batteries via an In Situ Conversion Route. *J. Mater. Chem.* **2011**, *21*, 10437−10441.

(25) Su, J.; Wu, X. L.; Yang, C. P.; Lee, J. S.; Kim, J.; Guo, Y. G. Self-Assembled $LiFePO_4$/C Nano/Microspheres by Using Phytic Acid as Phosphorus Source. *J. Phys. Chem. C* **2012**, *116*, 5019−5024.

(26) Cao, F. F.; Guo, Y. G.; Wan, L. J. Better Lithium-Ion Batteries with Nanocable-like Electrode Materials. *Energy Environ. Sci.* **2011**, *4*, 1634−1642.

(27) Xia, Y.; Zhang, W. K.; Huang, H.; Gan, Y. P.; Tian, J.; Tao, X. Y. Self-Assembled Mesoporous $LiFePO_4$ with Hierarchical Spindle-like Architectures for High-Performance Lithium-Ion Batteries. *J. Power Sources* **2011**, *196*, 5651−5658.

(28) Yang, H.; Wu, X. L.; Cao, M. H.; Guo, Y. G. Solvothermal Synthesis of $LiFePO_4$ Hierarchically Dumbbell-Like Microstructures by Nanoplate Self-Assembly and Their Application as a Cathode Material in Lithium-Ion Batteries. *J. Phys. Chem. C* **2009**, *113*, 3345−3351.

(29) Park, Y. J.; Shin, W.; Lee, J. W. Synthesis of Hollow Spherical $LiFePO_4$ by a Novel Route Using Organic Phosphate. *CrystEngComm* **2012**, *14*, 4612−4617.

(30) Zhang, C. J.; He, X.; Kong, Q. S.; Li, H.; Hu, H.; Wang, H. B.; Gu, L.; Wang, L.; Cui, G. L.; Chen, L. Q. A Novel Assembly of $LiFePO_4$ Microspheres from Nanoplates. *CrystEngComm* **2012**, *14*, 4344−4349.

(31) Yu, F.; Zhang, J. J.; Yang, Y. F.; Song, G. Z. Up-Scalable Synthesis, Structure and Charge Storage Properties of Porous Microspheres of $LiFePO_4$@C Nanocomposites. *J. Mater. Chem.* **2009**, *19*, 9121−9125.

(32) Dokko, K.; Koizumi, S.; Nakano, H.; Kanamura, K. Particle Morphology, Crystal Orientation, and Electrochemical Reactivity of $LiFePO_4$ Synthesized by the Hydrothermal Method at 443 K. *J. Mater. Chem.* **2007**, *17*, 4803−4810.

(33) Ellis, B.; Kan, W. H.; Makahnouk, W. R. M.; Nazar, L. F. Synthesis of Nanocrystals and Morphology Control of Hydrothermally Prepared $LiFePO_4$. *J. Mater. Chem.* **2007**, *17*, 3248−3254.
(34) Li, D.; Muller, M. B.; Gilje, S.; Kaner, R. B.; Wallace, G. G. Processable Aqueous Dispersions of Graphene Nanosheets. *Nat. Nanotechnol.* **2008**, *3*, 101−105.
(35) Xie, M.; Zhang, X. X.; Laakso, J.; Wang, H.; Levänen, E. New Method of Postmodifying the Particle Size and Morphology of $LiFePO_4$ via Supercritical Carbon Dioxide. *Cryst. Growth Des.* **2012**, *12*, 2166−2168.
(36) Song, Q. Z.; Ou, X. Q.; Wang, L.; Liang, G. C.; Wang, Z. R. Effect of pH Value on Particle Morphology and Electrochemical Properties of $LiFePO_4$ by Hydrothermal Method. *Mater. Res. Bull.* **2011**, *46*, 1398−1402.
(37) Xu, T. G.; Zhang, C.; Shao, X.; Wu, K.; Zhu, Y. F. Monomolecular-Layer $Ba_5Ta_4O_{15}$ Nanosheets: Synthesis and Investigation of Photocatalytic Properties. *Adv. Funct. Mater.* **2006**, *16*, 1599−1607.
(38) Burba, C. M.; Frech, R. Raman and FTIR Spectroscopic Study of Li_xFePO_4 ($0 \leq x \leq 1$). *J. Electrochem. Soc.* **2004**, *151*, A1032−A1038.
(39) Wu, X. L.; Jiang, L. Y.; Cao, F. F.; Guo, Y. G.; Wan, L. J. $LiFePO_4$ Nanoparticles Embedded in a Nanoporous Carbon Matrix: Superior Cathode Material for Electrochemical Energy-Storage Devices. *Adv. Mater.* **2009**, *21*, 2710−2714.
(40) Yang, J. L.; Wang, J. J.; Tang, Y. J.; Wang, D. N.; Li, X. F.; Hu, Y. H.; Li, R. Y.; Liang, G. X.; Sham, T. K.; Sun, X. L. $LiFePO_4$-Graphene as a Superior Cathode Material for Rechargeable Lithium Batteries: Impact of Stacked Graphene and Unfolded Graphene. *Energy Environ. Sci.* **2013**, *6*, 1521−1528.
(41) Chen, Y. M.; Lu, Z. G.; Zhou, L. M.; Mai, Y. W.; Huang, H. T. Hollow Carbon-Nanotube/Carbon-Nanofiber Hybrid Anodes for Li-Ion Batteries. *Energy Environ. Sci.* **2012**, *5*, 7898−7902.
(42) Oh, S. W.; Huang, Z. D.; Zhang, B.; Yu, Y.; He, Y. B.; Kim, J. K. Low Temperature Synthesis of Graphene-Wrapped $LiFePO_4$ Nanorod Cathodes by the Polyol Method. *J. Mater. Chem.* **2012**, *22*, 17215−17221.